nature nanotechnology
VOL.3 NO.4 APRIL 2008
www.nature.com/naturenanotechnology

Nanotubes go with the flow

NANOELECTRONICS
Into the terahertz regime

SELF ASSEMBLY
New directions for silicon

SCIENCE FICTION
Back to the future

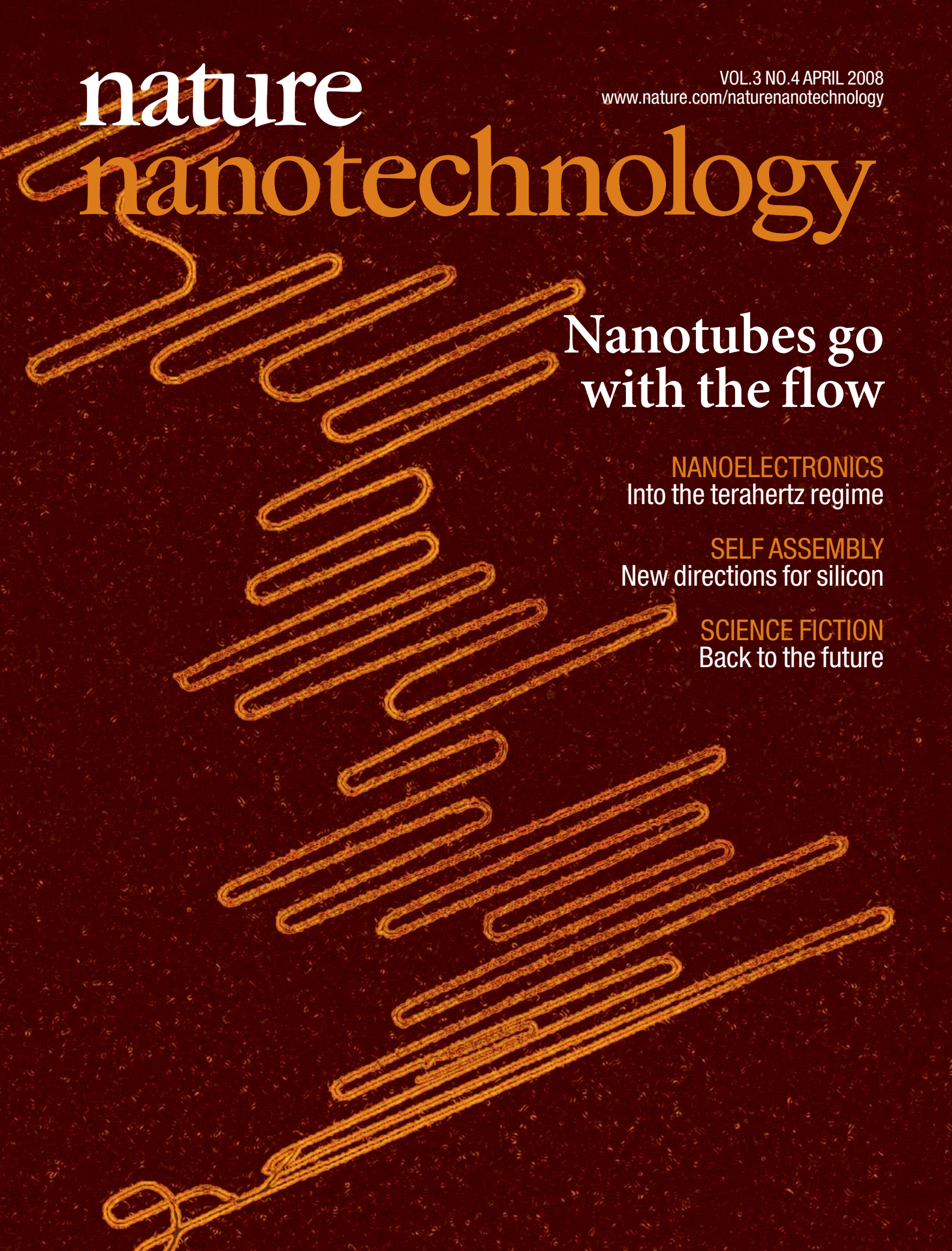

Self-organized nanotube serpentines

NOAM GEBLINGER†, ARIEL ISMACH† AND ERNESTO JOSELEVICH*

Department of Materials and Interfaces, Weizmann Institute of Science, Rehovot 76100, Israel
†These authors contributed equally to this work.
*e-mail: ernesto.joselevich@weizmann.ac.il

Published online: 30 March 2008; doi:10.1038/nnano.2008.59

Carbon nanotubes[1] have unique mechanical, electronic, optical and thermal properties, which make them attractive building blocks in the field of nanotechnology[2]. However, their organization into well-defined straight or curved geometries and arrays on surfaces remains a critical challenge for their integration into functional nanosystems. Here we show that combined surface- and flow-directed growth enable the controlled formation of uniquely complex and coherent geometries of single-walled carbon nanotubes, including highly oriented and periodic serpentines and coils. We propose a mechanism of non-equilibrium self-organization[3], in which competing dissipative forces of adhesion and aerodynamic drag induce oscillations in the nanotubes as they adsorb on the surface. Our results demonstrate the use of 'order through fluctuations'[3] to shape nanostructures into complex geometries. The nanotube serpentines and loops are shown to be electrically conducting and could therefore find a wide range of potential applications, such as receiving and transmitting antennas, heating and cooling elements, optoelectronic devices and single-molecule dynamos.

The spontaneous self-organization of complex structures from simple components is perhaps one of the most intriguing phenomena occurring in such vastly different fields as cosmology[4], geology[5], botany[6] and embryology[7], as well as chemistry and materials science[8]. It has long been recognized that whereas self-organization near thermodynamic equilibrium tends to attenuate fluctuations, leading to relatively simple geometries, self-organization far from equilibrium can amplify fluctuations into coherent oscillations, leading to much more complex geometries[3]. Notwithstanding its great potential implications for nanotechnology, this universal principle of 'order through fluctuations'[3] has not yet been widely applied to the self-assembly of complex structures at the nanoscale[8]. In particular, the prospect of nanoelectronic circuits and nanodevices based on carbon nanotubes[9] has stimulated extensive research on the organization of these one-dimensional nanostructures into well-defined geometries and arrays on surfaces.

One approach is the controlled deposition of pre-formed nanotubes from liquid suspension by means of tailored surfaces[10], fluidic flows[11] and electric fields[12]. A different approach involves the growth of nanotubes under the influence of electric fields[13] or gas flow[14]. A more recent and promising approach comprises guided growth on well-defined crystal surfaces by different modes of orientational epitaxy[15–19], where the nanotubes can be aligned by atomic steps on miscut sapphire (vicinal α-Al_2O_3 (0001))[15] or miscut quartz (vicinal α-SiO_2 $(1\bar{1}01)$)[19], by atomic rows on certain planes of sapphire (α-Al_2O_3 $(11\bar{2}0)$ or α-Al_2O_3 $(1\bar{1}02)$)[17,18], or by nanofacets on annealed miscut sapphire (vicinal α-Al_2O_3 (0001))[16]. Simultaneous combination of orientational epitaxy with field-directed growth has further enabled the self-assembly of nanotube crossbar architectures in a single growth step[20]. Although such straight configurations are desirable for the assembly of nanocircuits[21], one could envisage different devices based on curved and more complex geometries[22], which cannot be obtained by simple mechanisms of aligned growth.

Controlled formation of complex nanotube geometries, such as rings and loops, has been achieved by directed assembly of pre-formed nanotubes, using affinity templates[23] and microfluidics[24]. However, surface-directed growth has so far only yielded nanotubes that are straight and parallel to the atomic steps, atomic rows or nanofacets, although kinked[15] and wavy[16] nanotubes have also been templated by kinked atomic steps and sawtooth nanofacets, respectively. In all cases, the alignment was solely determined by the surface, and not affected by external forces such as electric fields or gas flow. These facts are consistent with a surface-bound growth mechanism, where each catalyst nanoparticle slides along the surface guide, leaving the nanotube behind as a wake[15,16]. Thus, the nanotubes reached the minimum-energy configuration by simply reproducing the shape of the underlying surface features, without a significant addition of complexity to the system.

Here we present an intriguing new type of nanotube structures strikingly more complex than those observed before. We first noticed a few serpentines, such as the one shown in Fig. 1a, in some of our samples of single-walled carbon nanotubes grown on miscut quartz (see Supplementary Information). Each serpentine consisted of a series of straight, parallel and regularly spaced segments, connected by alternating U-turns. The straight segments were parallel to the surface steps of the vicinal α-SiO_2 $(1\bar{1}01)$ surface, in the $[11\bar{2}0]$ direction, and the serpentines propagated in the direction of the gas flow, which was perpendicular to the steps. Occasionally, full nanotube loops could also be observed (Fig. 1a). The formation of these structures, which were determined by both the surface and the flow, could not be explained by the previous wake-growth mechanism[15,16]. We hypothesized that the serpentines could form in a two-step mechanism, where the nanotubes first grow standing up from the surface, and at a later stage adsorb on the surface in an oscillatory fashion along the steps, like spaghetti falling on a tilted bamboo mat (Fig. 1g).

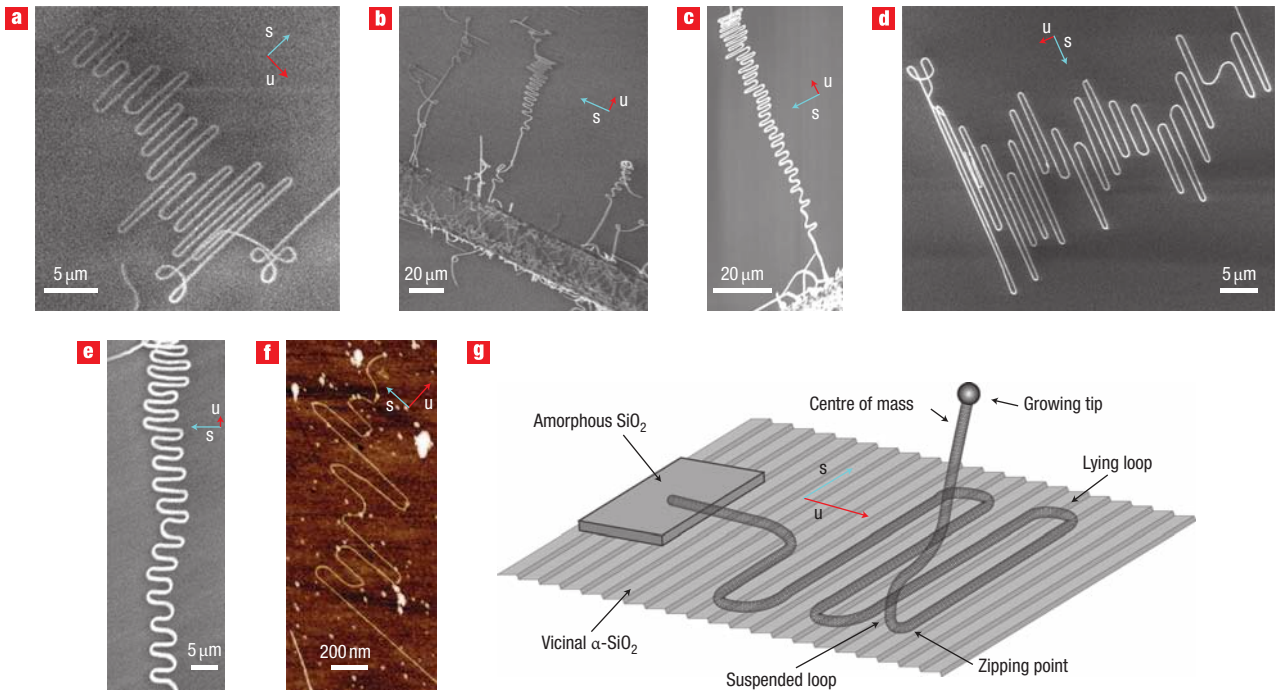

Figure 1 Representative nanotube serpentines. a–f, The samples were obtained under different conditions, observed by SEM (**a–e**) and AFM (**f**). The directions of the steps and flow are indicated by the step vector[15] **s** and the flow vector **u**, respectively. Unless otherwise stated, standard growth conditions are as described in the Methods ($u = 1{,}000$ s.c.c.m., $t = 10$ min). **a**, Occasional serpentine (low yield) grown on bare quartz. **b**, Several serpentines grown at higher yield from amorphous SiO_2 stripes ($u = 500$ s.c.c.m., $t = 30$ min). **c**, A long serpentine ($u = 500$ s.c.c.m., $t = 20$ min). **d**, Wide and dense serpentine ($u = 500$ s.c.c.m., $t = 60$ min), obtained at very high yield from evaporated Fe on amorphous SiO_2. **e**, Long, narrow and highly periodic serpentine ($u = 250$ s.c.c.m., $t = 20$ min). **f**, Topographic AFM image of a very small serpentine, average parallel section length $W = 280 \pm 175$ nm, average U-turn diameter $D = 74 \pm 10$ nm, nanotube diameter $d = 0.9 \pm 0.1$ nm (on bare miscut quartz). **g**, Schematic representation of the 'falling spaghetti' mechanism (see Supplementary Information, movie).

To test this hypothesis and increase the yield of serpentines, we made use of our previous knowledge that an amorphous SiO_2 coating inhibits surface-bound growth and promotes the growth of standing nanotubes[15,20]. We therefore patterned the catalyst nanoparticles (ferritin or evaporated Fe) on stripes or islands of amorphous SiO_2 parallel to the steps, and then grew single-walled carbon nanotubes with the gas flow perpendicular to the steps. This indeed produced a high yield of nanotube serpentines (tens to thousands per sample), as shown in Fig. 1b (see also Supplementary Information, Fig. S7). As exemplified in Fig. 1c, the serpentines usually start from the amorphous SiO_2 stripes as a straight segment along the flow direction, followed by a transitional region of disordered serpentine, which becomes gradually more periodic and regular. Depending on the growth conditions, serpentines can be relatively wide, short and dense (width $W = 10–30$ μm, length $L = 20–200$ μm), as in Fig. 1d, or relatively narrow, long and highly periodic ($W = 3–10$ μm, $L = 100–1{,}000$ μm), as in Fig. 1e. The diameter D of the U-turns, which is also the spacing between the straight segments, normally ranges between 0.5 and 8 μm, although a few serpentines can have very small U-turn diameters ($D = 75–100$ nm), as shown in Fig. 1f, in which case the U-turns may be kinked at one or two points. As seen in Fig. 1c–e, serpentines often become slightly wider and denser toward their end (see Supplementary Information, Figs S1 and S2, for quantitative data and additional images). The catalyst nanoparticle can usually be observed at the end of the serpentine (see Supplementary Information, Fig. S3), suggesting that the nanotube elongates from its upper tip rather than from its base. Atomic force microscopy (AFM, see Fig. 3), transmission electron microscopy (TEM; see Supplementary Information, Fig. S4) and Raman spectroscopy (see Supplementary Information, Fig. S5) show that at least 90% of the nanotubes are single-walled, of diameters d ranging from 0.8 to 4 nm, although a few double-walled carbon nanotubes could also be found.

With these observations, we can intuitively describe our proposed 'falling spaghetti mechanism' (Fig. 1g) in the following way (see Supplementary Information for an animated movie and further discussion). The first stage is the regular tip-growth of a suspended nanotube[14], which may take several minutes, depending on the growth time. Once the nanotube has grown to a considerable length, this growth process is followed by a rapid oscillatory fall process, in which the serpentine shape is generated. In the fall process the nanotube adsorbs onto the surface by tangentially zipping down, from base to tip, preferentially along a surface step. The zipping motion pulls the lower region of the nanotube away from its centre of mass, while a drag force pulls its upper region in the opposite sense, causing the formation of a suspended loop tangent to the surface. The zipping point propagates farther away along the step until the opposed drag force is enough to derail the nanotube from the step. This causes an instability that leads to a change in the direction of zipping, and the fall of the suspended loop on the surface, preferentially in the direction of the flow, thus forming a U-turn. The zipping then continues in an antiparallel direction along another surface step. The same process repeats itself again and again in an oscillatory way, until the entire length of the nanotube has adsorbed onto the surface in the form of a serpentine. Occasionally, if the suspended loop falls against the

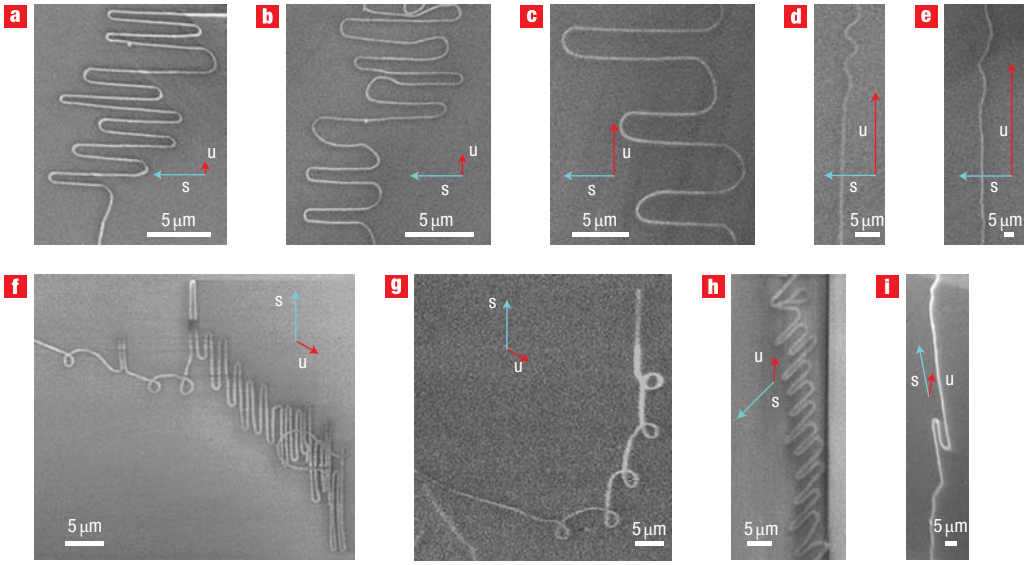

Figure 2 Flow rate and direction effects on serpentine shape. a–e, SEM images of serpentines grown at different flow rates: $u = 250$ s.c.c.m. (**a**); $u = 500$ s.c.c.m. (**b**); $u = 1{,}000$ s.c.c.m. (**c**); $u = 1{,}500$ s.c.c.m. (**d**); $u = 2{,}000$ s.c.c.m. (**e**). As the flow rate increases, the parallel segments become shorter and more spaced (that is, larger U-turn diameters). Further increasing the flow rate (**d**,**e**) inhibits serpentine formation. **f–i**, SEM images of serpentines grown with the flow at different angles from the steps: $\alpha = 64°$ (**f**), showing a typical skewed serpentine with several loops ($d = 2.0 \pm 0.2$ μm); $\alpha = 64°$ (**g**, same sample as in **f**), showing a nanotube coil of five connected full loops; $\alpha = 42°$ (**h**), showing a highly skewed serpentine; $\alpha = 9°$ (**i**), showing a straight nanotube with sigmoid deformation.

flow direction, it makes a round loop instead of a U-turn, as seen in Fig. 1a. This oscillatory fall process is driven by a strong nanotube–surface adhesion, which is countered by the aerodynamic drag and the elastic behaviour of the nanotube, and can be much faster than the growth process.

The gas flow rate and direction have significant effects on the shape of the nanotube serpentines (Fig. 2). As shown in Fig. 2, increasing the flow rate from 250 to 1,000 s.c.c.m. (Fig. 2a–c) leads to a gradual increase of the average U-turn diameter (serpentine spacing) from 0.8 to 4 μm. A higher flow rate (~1,500 s.c.c.m.; Fig. 2d) leads to disordered serpentines, and even higher flow rates (2,000 s.c.c.m. and higher; Fig. 2e) completely inhibit the formation of serpentines, yielding straight nanotubes along the flow direction. Interestingly, suddenly increasing the flow rate from 250 s.c.c.m. to 1,300 s.c.c.m. after switching off the carbon feedstock gas yields both serpentines and straight flow-directed nanotubes (see Supplementary Information, Fig. S8). This indicates that the serpentine fall is independent of the nanotube growth, providing further support to our proposed two-step mechanism. We have not observed a significant effect of using different miscut angles of vicinal quartz. Moreover, we have also observed serpentines on vicinal sapphire (see Supplementary Information, Fig. S9), although less frequently than on vicinal quartz.

Changing the direction of flow with respect to the steps from 90° to smaller angles has a notable qualitative effect, as shown in Fig. 2f–i. When the angle α between the flow and the steps is between 40° and 70° (Fig. 2f–h), we obtain mostly skewed serpentines (31–36% of the observed nanotubes) with a large number of round loops (6–27%), and also a significant number of flat coils (6–9%), each consisting of a series of round loops connected by straight segments (Fig. 2g; see also Supplementary Information, Fig. S6). The skewed serpentines can have left and right U-turns of different diameters (Fig. 2h). The diameters of the round loops are relatively uniform for each nanotube coil, varying between 0.5 and 5 μm from one nanotube to another. At small angles ($\alpha < 10°$, Fig. 2i), the skewed serpentines become mostly straight nanotubes (39%), with kinks (31%) or occasional sigmoid deformations (19%) leaning toward the flow direction.

Besides these flow effects, the U-turn diameter (serpentine spacing) is found to correlate with the nanotube diameter, as revealed by studying the shape and topography of the same serpentines by scanning electron microscopy (SEM) and AFM, respectively (Fig. 3). As an example, Fig. 3a shows two neighbouring serpentines with different nanotube diameters. Although the two serpentines have grown in exactly the same conditions, and even cross each other twice, each serpentine has a different typical U-turn diameter, which correlates with its nanotube diameter (Fig. 3b–g). The nanotube diameter measured by AFM is constant along each serpentine, as confirmed also by Raman measurements (see Supplementary Information, Fig. S5). A detailed statistical study of 10 serpentines grown at three different flow rates reveals a roughly linear correlation between serpentine U-turn diameter D and nanotube diameter d (Fig. 3h; see also Supplementary Information, Fig. S6), with a slightly different factor depending on the flow rate. This correlation is consistent with the higher mechanical stiffness of wider nanotubes, and also with the general flow rate effect described in Fig. 2a–e.

Analysing the shape of the serpentines from a mechanical and aerodynamic point of view allows us to make some interesting rough estimations regarding the falling-spaghetti mechanism (see Supplementary Information for details). First, the diameters of the serpentine U-turns and coil loops (for example, $D = 2.1$ μm and 3.2 μm for the two serpentines in Fig. 3a) are more than one order of magnitude smaller than the persistence length of the nanotubes[25] (25 μm and 145 μm, respectively), and can sometimes be significantly smaller than random loops previously

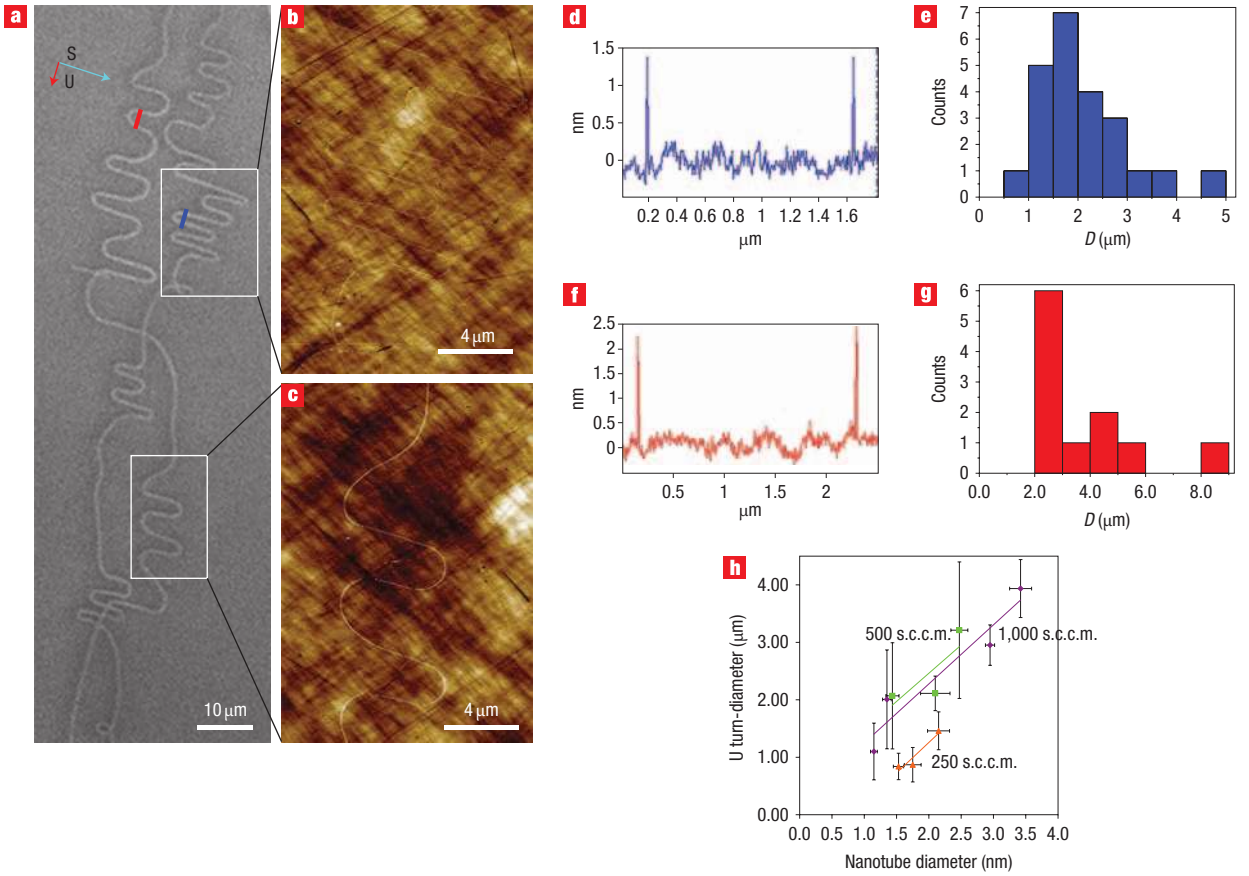

Figure 3 Nanotube diameter effect on serpentine shape. a, SEM image of two nearby nanotube serpentines ($u = 500$ s.c.c.m.). **b**,**c**, AFM images of the selected areas in the SEM micrograph showing parts of the two serpentines. Height scale, 2.5 nm. **d**,**f**, Topographic section profiles of low-scale topographic AFM images taken at places marked on the SEM micrograph (**a**). The height of the peaks represents the nanotube diameter, and the distance between the peaks represents the U-turn diameter. Upper nanotube diameter (blue), $d = 1.4 \pm 0.1$ nm; lower nanotube diameter (red), $d = 2.5 \pm 0.1$ nm. **e**,**g**, Histograms representing the U-turn diameter D distribution for the upper (**e**) and lower (**g**) serpentines. **h**, Plot of U-turn diameter as a function of nanotube diameter d. The data were collected for 10 serpentines (4 serpentines in a sample grown at $u = 1{,}000$ s.c.c.m. (purple), 3 serpentines in a sample grown at $u = 500$ s.c.c.m. (green), and 3 serpentines in a sample grown at $u = 250$ s.c.c.m. (orange)). The vertical error bars represent the standard deviation from tens of U-turns for each serpentine (see Supplementary Information for exemplary statistical data, Fig. S6).

observed[22]. Second, from these U-turn diameters we can estimate the pulling force attributed to the drag to be 0.17 pN and 0.41 pN, respectively. This is three orders of magnitude smaller than the expected driving force for zipping due to surface–nanotube van der Waals interactions[26]; that is, ~ 2 eV nm$^{-1} = 320$ pN. Third, assuming a classical drag, we can roughly estimate the zipping velocity for a typical serpentine to range from 1 to 7 m s^{-1}, which means that the fall of the serpentine takes 300–50 μs, with an oscillation frequency of 50–300 kHz. Hence, the nanotube fall is indeed much faster than its growth.

These estimations underscore how far the self-organized serpentines and coils are from equilibrium, and how much energy is dissipated during their formation relative to their final state. This may have implications in the emerging field of non-equilibrium ('dynamic') self-assembly[8], illustrating how dissipative forces and kinetic barriers can lead to the spontaneous generation of much more complex patterns than those generated by the more common equilibrium ('static') self-assembly processes. Although the serpentines eventually become kinetically trapped on the surface, they have the characteristics of dissipative structures[3], because during their formation their active part is far from equilibrium, in a way that allows for the amplification of fluctuations into coherent spatiotemporal oscillations, like in an oscillatory chemical reaction[27]. This system leaves ground for interesting simulations and theoretical studies.

A preliminary characterization of the electrical properties of the nanotube serpentines by electrostatic force microscopy (EFM)[28] and transport measurements is shown in Fig. 4. EFM imaging of entire nanotube serpentines connected at one end (Fig. 4a–e) reveals that the serpentines are conducting through their full length, with no breaks and no appreciable drop in the potential along the serpentine. This is consistent with the low density of structural defects revealed by Raman spectroscopy (see Supplementary Information, Fig. S5). The resistance of 10-μm serpentine segments was around 2 MΩ (Fig. 4f), which is still quite high, but this may be due to poor contacts. Resistances across 1–2-μm segments of serpentines can vary from several MΩ to as little as 35 kΩ (see Supplementary Information, Fig. S12), which is not too far from the ballistic transport regime[2,9]. In principle, entire serpentines could be highly conductive, as recent studies have shown well-aligned single-walled carbon nanotubes on similar vicinal quartz substrates to

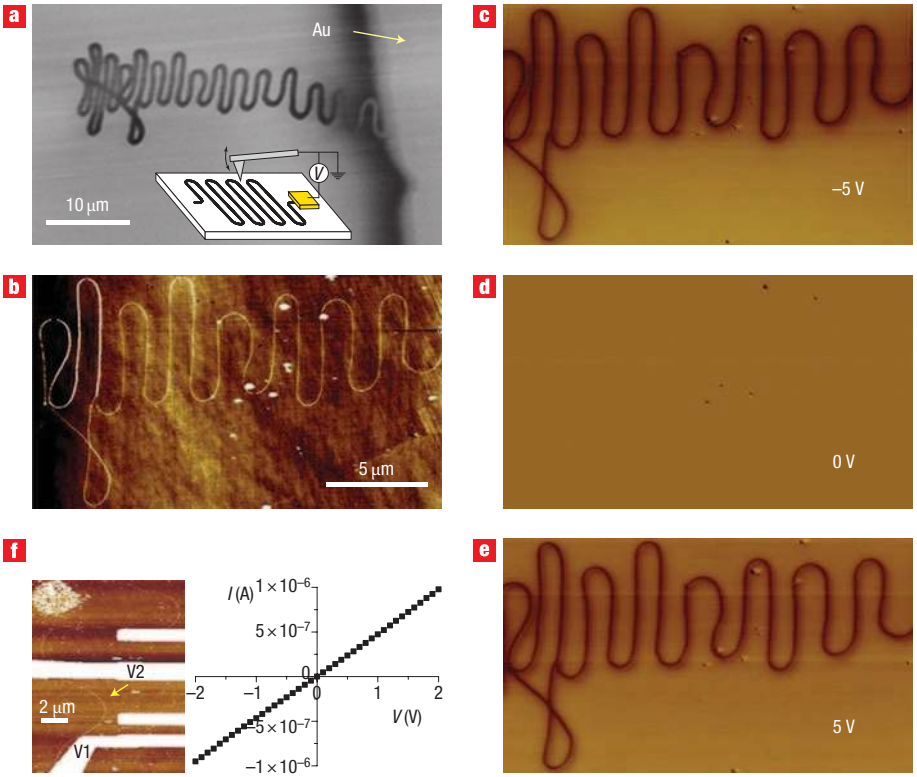

Figure 4 Electrical characterization of nanotube serpentines. a, SEM image of a serpentine connected to an electrode (Au) at one end. Inset: schematic EFM setup. **b**, Topographic image of the same serpentine ($d = 1.5 \pm 0.2$ nm). **c**–**e**, EFM imaging of the serpentine while applying a bias of -5 V (**c**), 0 V (**d**) and 5 V (**e**) to the electrode, tip grounded. Positive and negative bias led to a similar EFM signal (**c** and **e**, respectively), and the signal disappears at 0 V (**d**) (see also Supplementary Information, Fig. S11). The topographic image (**b**) remains the same for all applied bias values. **f**, Transport measurement on a serpentine (yellow arrow) with nanotube diameter $d = 3.5 \pm 0.2$ nm. The topographic AFM image (left) shows the serpentine attached to Pd contacts (white). The I–V curve (right) is between V1 and V2, showing a resistance of 2 MΩ for a serpentine segment of ~10 μm.

have very high mobilities[29]. Further electrical characterizations of nanotube serpentines are currently under way.

From a practical point of view, it is interesting to note that serpentines are a common geometry in many functional systems, such as antennas, radiators, collectors, heating and cooling elements, as well as for lighting, irrigation, and so on. Analogously, we can envisage that nanotube serpentines could find a wide range of nanodevice applications, such as transmitting and receiving antennas of electromagnetic radiation[30] (size-resonant in the terahertz region), heating and cooling elements (for example, for cooling electronic circuits) and optoelectronic devices (such as sensitive infrared detectors). In addition, nanotube loops could be the basis for power-generating single-molecule dynamos.

Received 24 September 2007; accepted 19 February 2008; published 30 March 2008.

References

1. Iijima, S. Helical microtubules of graphitic carbon. *Nature* **354,** 56–58 (1991).
2. Jorio, A., Dresselhaus, M. S. & Dresselhaus, G. (eds) *Carbon Nanotubes: Advanced Topics in the Synthesis, Structure, Properties and Applications.* Series: Topics in Applied Physics, Vol. 111 (Springer, Heidelberg, 2008).
3. Nicolis, G. & Prigogine, I. *Self-Organization in Non-Equilibrium Systems: From Dissipative Structures to Order through Fluctuations* (John Wiley, New York, 1977).
4. Springel, V., Frenk, C. S. & White, S. D. M. The large-scale structure of the Universe. *Nature* **440,** 1137–1144 (2006).
5. Werner, B. T. Complexity in natural landform patterns. *Science* **284,** 102–104 (1999).
6. Vollbrecht, E. *et al.* Architecture of floral branch systems in maize and related grasses. *Nature* **436,** 1119–1126 (2005).
7. Lumelsky, N. *et al.* Differentiation of embryonic stem cells to insulin-secreting structures similar to pancreatic islets. *Science* **292,** 1389–1394 (2001).
8. Whitesides, G. M. & Grzybowski, B. Self-assembly at all scales. *Science* **295,** 2418–2421 (2002).
9. Avouris, P. Molecular electronics with carbon nanotubes. *Acc. Chem. Res.* **35,** 1026–1034 (2002).
10. Liu, J. *et al.* Controlled deposition of individual single-walled carbon nanotubes on chemically functionalized templates. *Chem. Phys. Lett.* **303,** 125–129 (1999).
11. Diehl, M. *et al.* Self-assembled, deterministic carbon nanotube wiring networks. *Angew. Chem. Int. Edn* **41,** 353–356 (2001).
12. Krupke, R., Hennrich, F., von Lohneysen, H. & Kappes, M. M. Separation of metallic from semiconducting single-walled carbon nanotubes. *Science* **301,** 344–347 (2003).
13. Joselevich, E. & Lieber, C. M. Vectorial growth of metallic and semiconducting single-wall carbon nanotubes. *Nano Lett.* **2,** 1137–1141 (2002).
14. Huang, S., M. Cai, X. Y. & Liu, J. Growth of millimeter-long and horizontally aligned single-walled carbon nanotubes on flat substrates. *J. Am. Chem. Soc.* **125,** 5636–5637 (2003).
15. Ismach, A., Segev, L., Wachtel, E. & Joselevich, E. Atomic-step-templated formation of single wall carbon nanotube patterns. *Angew. Chem. Int. Edn* **43,** 6140–6143 (2004).
16. Ismach, A., Kantorovich, D. & Joselevich, E. Carbon nanotube graphoepitaxy: Highly oriented growth by faceted nanosteps. *J. Am. Chem. Soc.* **127,** 11554–11555 (2005).
17. Han, S., Liu, X. L. & Zhou, C. W. Template-free directional growth of single-walled carbon nanotubes on a- and r-plane sapphire. *J. Am. Chem. Soc.* **127,** 5294–5295 (2005).
18. Ago, H. *et al.* Aligned growth of isolated single-walled carbon nanotubes programmed by atomic arrangement of substrate surface. *Chem. Phys. Lett.* **408,** 433–438 (2005).
19. Kocabas, C. *et al.* Guided growth of large-scale, horizontally aligned arrays of single-walled carbon nanotubes and their use in thin-film transistors. *Small* **1,** 1110–1116 (2005).
20. Ismach, A. & Joselevich, E. Orthogonal self-assembly of carbon nanotube crossbar architectures by simultaneous graphoepitaxy and field-directed growth. *Nano Lett.* **6,** 1706–1710 (2006).
21. Rueckes, T. *et al.* Carbon nanotube-based nonvolatile random access memory for molecular computing. *Science* **289,** 94–97 (2000).
22. Refael, G., Heo, J. S. & Bockrath, M. Sagnac interference in carbon nanotube loops. *Phys. Rev. Lett.* **98,** 246803 (2007).
23. Wang, Y. *et al.* Controlling the shape, orientation, and linkage of carbon nanotube features with nano affinity templates. *Proc. Natl Acad. Sci. USA* **103,** 2026–2031 (2006).
24. Tsukruk, V., Ko, H. & Peleshanko, S. Nanotube surface arrays: Weaving, bending, and assembling on patterned silicon. *Phys. Rev. Lett.* **92,** (2004).

25. Duggal, R. & Pasquali, M. Dynamics of individual single-walled carbon nanotubes in water by real-time visualization. *Phys. Rev. Lett.* **96,** 246104 (2006).
26. Hertel, T., Walkup, R. E. & Avouris, P. Deformation of carbon nanotubes by surface van der Waals forces. *Phys. Rev. B* **58,** 13870–13873 (1998).
27. Kurin-Csorgei, K., Epstein, I. R & Orban, M. Systematic design of chemical oscillators using complexation and precipitation equilibria. *Nature* **433,** 139–142 (2005).
28. Bachtold, A. *et al*. Scanned probe microscopy of electronic transport in carbon nanotubes. *Phys. Rev. Lett.* **84,** 6082–6085 (2000).
29. Kang, S. *et al*. High-performance electronics using dense, perfectly aligned arrays of single-walled carbon nanotubes. *Nature Nanotech.* **2,** 230–236 (2007).
30. Wang, Y. *et al*. Receiving and transmitting light-like radio waves: Antenna effect in arrays of aligned carbon nanotubes. *Appl. Phys. Lett.* **85,** 2607–2609 (2004).

Acknowledgements

This research was supported by the Israel Science Foundation, the US–Israel Binational Science Foundation, the Kimmel Center for Nanoscale Science, and the Djanogly, Alhadeff and Perlman Family foundations. E.J. holds the Victor Erlich Career Development Chair. We thank A. Jorio, G. Cançado and L. Novotny for Raman characterization, R. Popovitz-Biro for TEM characterization, A. Yoffe for assistance with the cleanroom facilities, R. Naaman for allowing us to use his electrical probe station, and N. Gov, K.S. Nagapriya and T. Yarden for helpful discussions.
Correspondence and requests for materials should be addressed to E.J.
Supplementary information accompanies this paper on www.nature.com/naturenanotechnology.

Self-organized nanotube serpentines

Noam Geblinger[*], Ariel Ismach[*] & Ernesto Joselevich[‡]

Department of Materials and Interfaces, Weizmann Institute of Science, Rehovot 76100, Israel.

20 September 2007

Supplementary Information

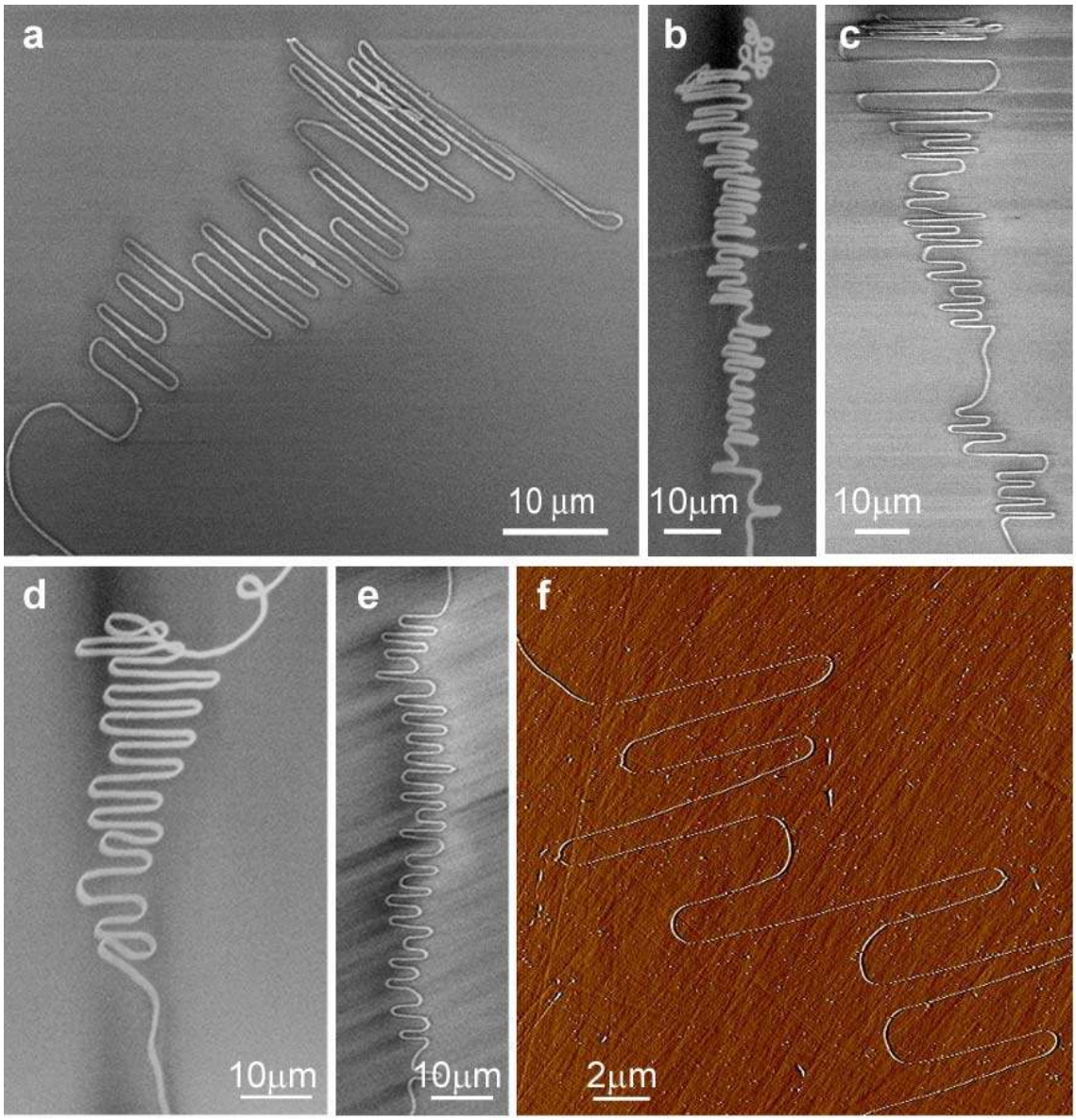

Figure S1. Additional nanotube serpentines obtained under different conditions, observed by SEM (**a-e**) and AFM (**f**). Standard growth conditions (unless otherwise stated) are as described in Fig. 1. **a,** u = 250 sccm. **b,** u = 500 sccm, t = 60 min. **c,** u = 500 sccm, t = 30 min. **d,** same sample as b. **e,** u = 500 sccm, t = 30 min. **f,** Amplitude AFM image (height scale 120 mV), same sample as **c**.

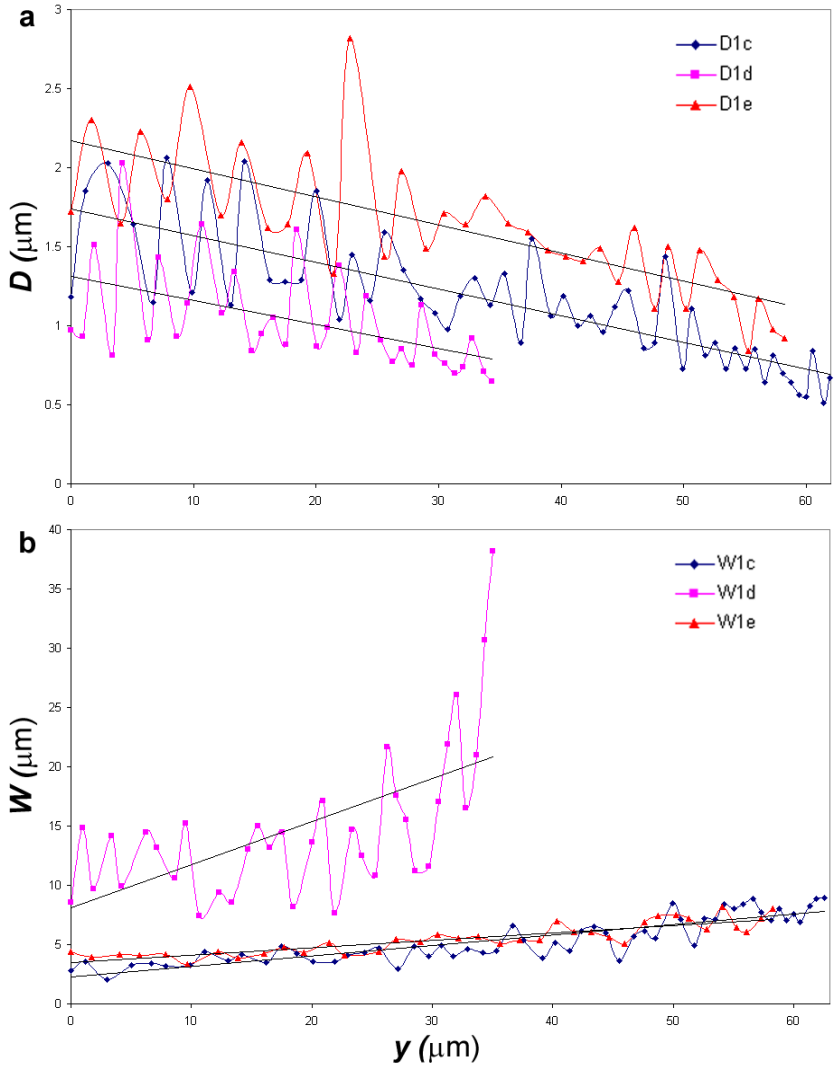

Figure S2. Gradual changes of period and width along the serpentine. **a**, Graph showing the gradual decrease of U-turn diameter (*D*) along the serpentine, as a function of the distance across the steps (*y*). **b**, Graph showing the gradual increase of width (*W*) along the serpentine, as a function of the distance across the steps (*y*). Both graphs are plotted for the three serpentines shown in Figs 1c,d and e. For all the three serpentines, the spacing decrease rate (slope of *D vs. y*) is 0.016 ± 0.001. For the two more regular serpentines (Fig. 1c,e), the width increase rate (slope of *W vs. y*) is 0.07 ± 0.01, corresponding to a spread angle of 4.0º ± 0.3º.

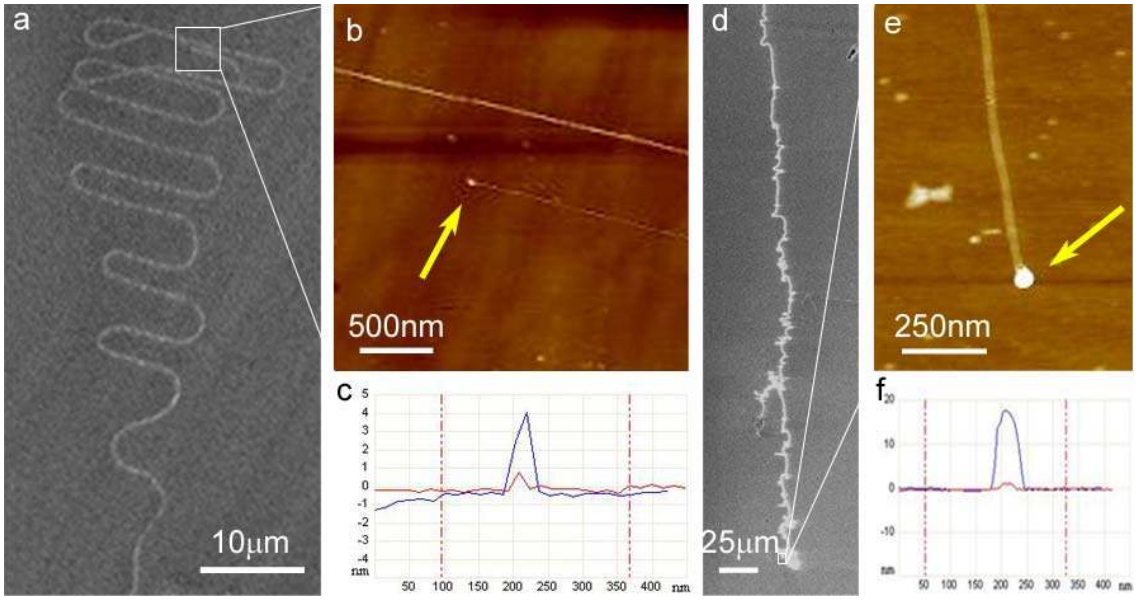

Figure S3. Catalyst nanoparticles at the ends of serpentines. **a**, SEM image of a nanotube serpentine. **b**, Topographic AFM image of the selected area in the SEM micrograph showing the end of the serpentine which is far from the patterned stripe of amorphous SiO_2 and catalyst. The catalyst nanoparticle (yellow arrows) can be observed at the end of the serpentine, indicating a "tip-growth" mechanism of the nanotube. **c,** Topographic section profiles taken across the nanotube (red) and the particle (blue), exhibiting diameters of d = 1.0 ± 0.1 nm and 4.5 ± 0.2 nm respectively. **d-f,** Similar study done at the end of a longer nanotube serpentine, exhibiting diameters of d = 1.3 ± 0.1 nm for the nanotube and 18.3 ± 0.3 nm for the catalyst nanoparticle.

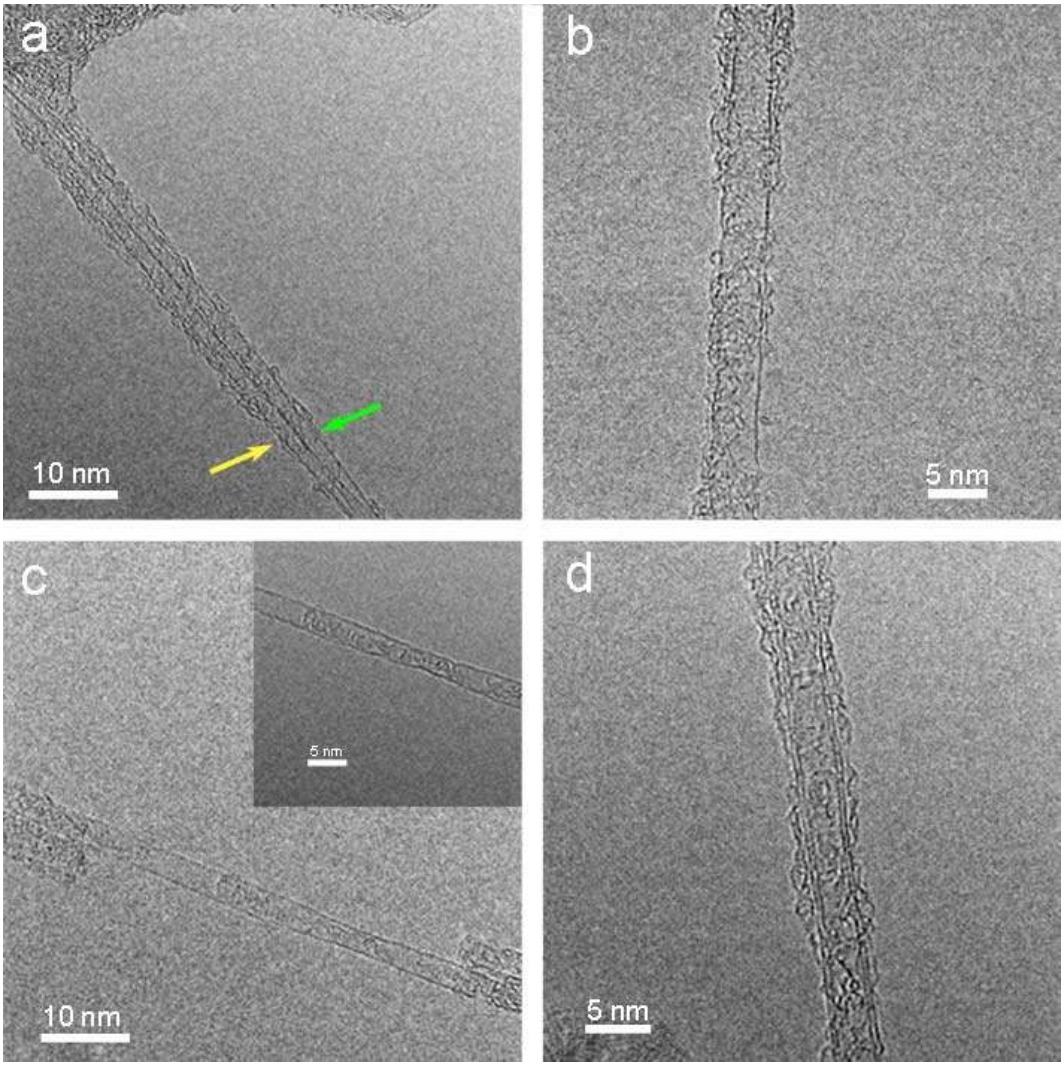

Figure S4. Nanotube *ex situ* characterization by TEM. a, High-resolution TEM image of two single-wall carbon nanotubes with diameters $d = 1.6 \pm 0.1$ nm and 1.8 ± 0.1 nm (yellow and green arrows respectively). **b** and **c**, SWNTs with $d = 3.9 \pm 0.1$ nm and 2.7 ± 0.1 nm, respectively. The inset in **c** displays an image taken a few minutes later, showing that defects are caused by the electron beam. **d**, Double-wall carbon nanotube (DWNT) with inner and outer diameters 2.7 ± 0.1 nm and 3.4 ± 0.1 nm, respectively. More than 20 nanotubes extracted from our serpentines samples were characterized by HRTEM; only 2 were DWNTs; all the rest were SWNTs.

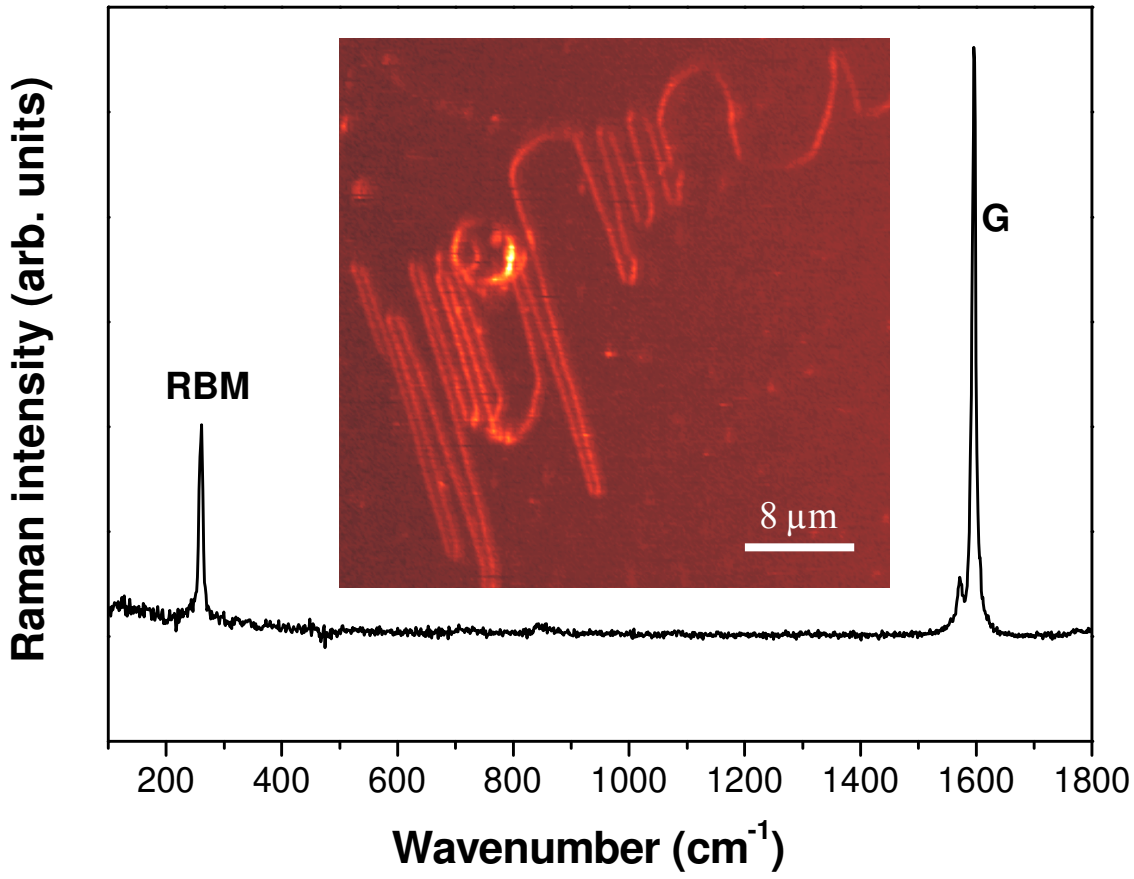

Figure S5. Nanotube *in situ* characterization by Raman spectroscopy. Raman spectrum and confocal image (G-band intensity) of a nanotube serpentine on vicinal quartz (laser wavelength: λ_{laser} = 785 nm, E_{laser} = 1.58 eV). The radial breathing mode (RBM) frequency is constant along the entire serpentine, ν_{RBM} = 260 cm^{-1}, which corresponds to a nanotube diameter d = 0.9 nm. The nanotube is thus identified as a semiconducting (n,m) = (10,2) through its entire length. The G-band frequency fluctuates between 1594 to 1603 cm^{-1}, perhaps due to changes in local stress or nanotube-surface interactions. The narrow Raman lines ($FWHM$ = 10 cm^{-1}) and the lack of D-band (~ 1300 cm^{-1}), indicate a very low density of structural defects. Hence, there are no changes in nanotube diameter and chirality along the serpentine. Similar data were obtained for other serpentines (L. G. Cançado, N. Geblinger, A. Ismach, E. Joselevich, A. Jorio and L. Novotny, *in preparation*).

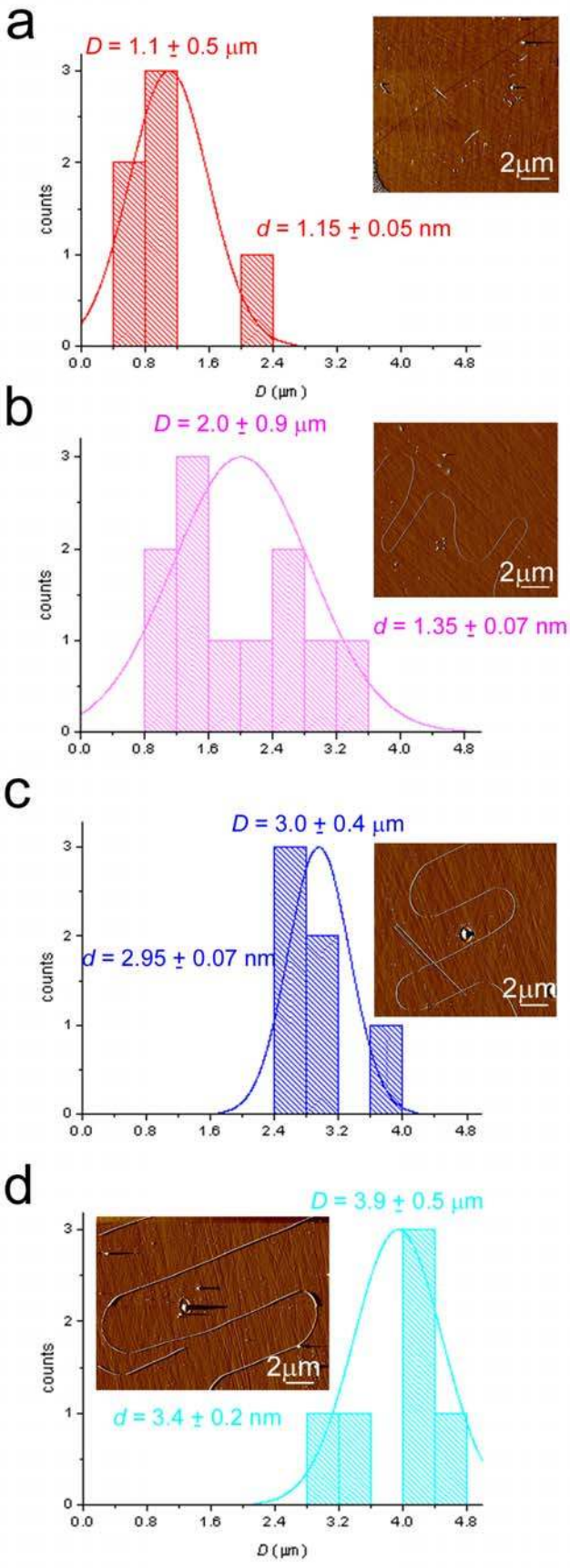

Figure S6. Exemplary statistical data relating the serpentine U-turn diameter to the nanotube diameter. Histograms representing the U-turn diameter (*D*) distribution for four serpentines with different nanotube diameter (*d*) grown under the same conditions; *u* = 1000. Inset in each histogram show a reprehensive AFM image of a segment of the given serpentine. As can be seen, both from the shift in the distribution and from the images, the average U-turn diameter increases with increasing nanotube diameter. These data are represented in Fig. 3h (purple plot).

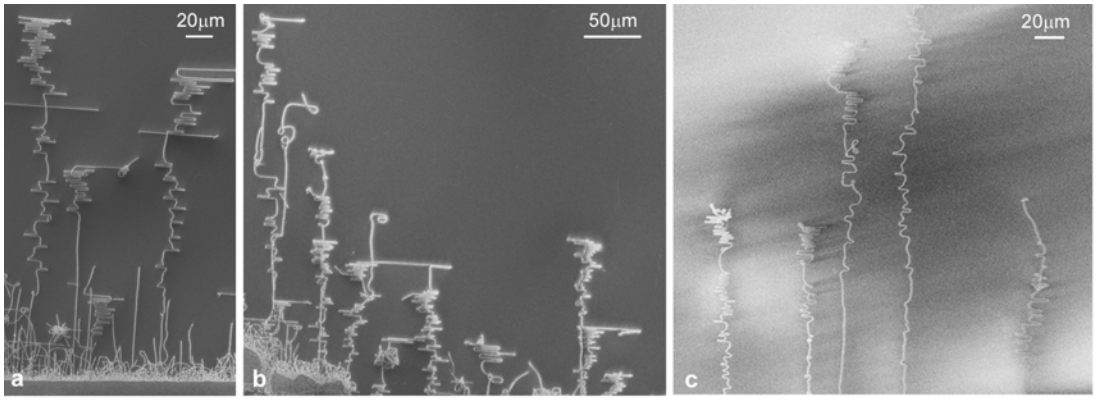

Figure S7. High-yield growth of nanotube serpentines from lithographic stripes of evaporated Fe/SiO_2 (**a**, **b**), and ferritin on evaporated SiO_2 (**c**). Growth conditions: *u*=500 sccm, *t*=60 min.

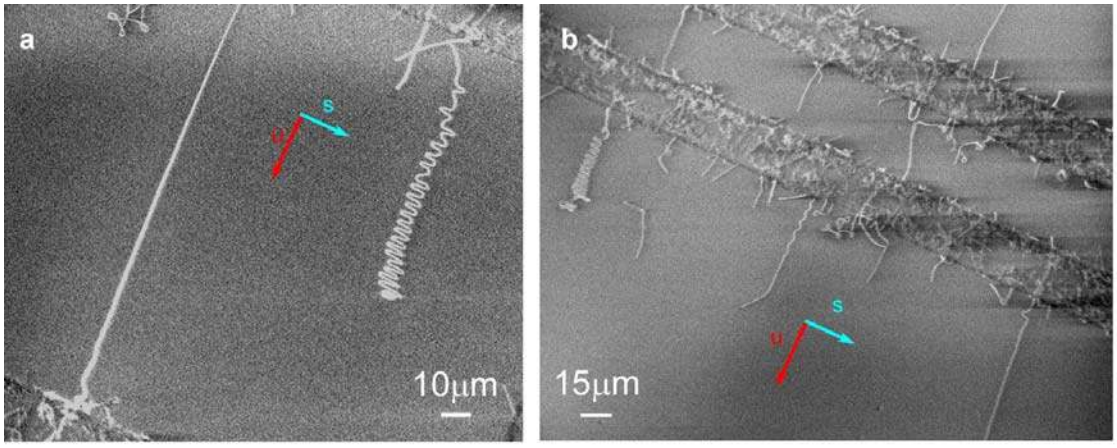

Figure S8. Stop-flow / inhibition experiment showing the independence of the nanotube growth and 'fall' stages. Nanotube growth was carried out at u = 250 sccm for t = 20 min., after which the carbon feedstock gas (C_2H_4) was switched off and the flow rate (of the Ar and H_2 mixture) was increased to u' = 1300 sccm. Both serpentines and straight flow-directed nanotubes can be observed, indicating that some nanotubes 'fell' during growth, while others fell after the growth was terminated.

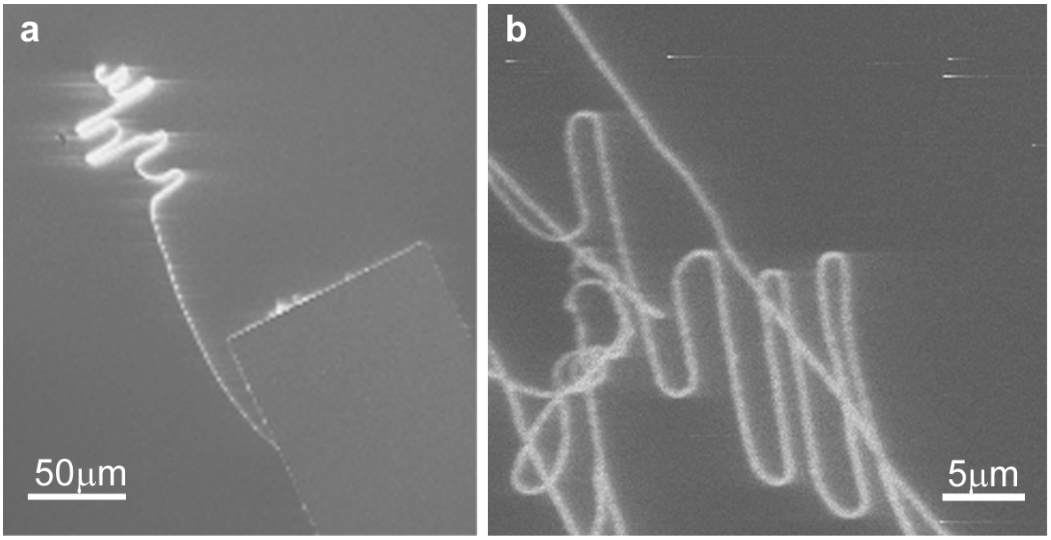

Figure S9. Nanotube serpentines formed on miscut sapphire. **a**, Vicinal α-Al_2O_3 (0001), 2º off-plane toward the $[11\bar{2}0]$ direction, u = 500 sccm, t = 60 min. **b**, Vicinal α-Al_2O_3 (0001), 4º off-plane toward the $[11\bar{2}0]$ direction, from evaporated Fe, u = 500 sccm, t = 60 min.

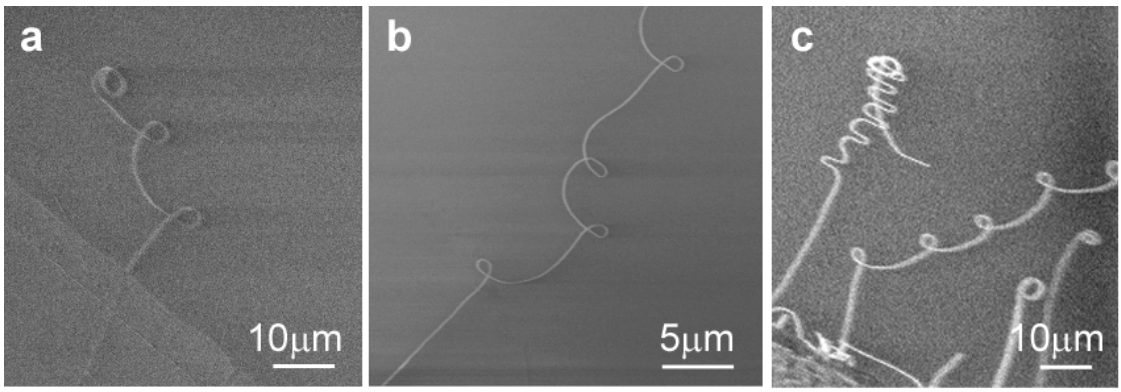

Figure S10. Additional nanotube coils, consisting of a series of round loops, observed by SEM. Partial alignment along surface steps can be noticed. **a,** u = 250 sccm, average loop diameter d = 1.54 ± 0.06 μm. **b,** same sample as **a**, d = 1.6 ± 0.2 μm. **c,** u = 500 sccm, t = 30 min, d = 2.0 ± 0.2 μm.

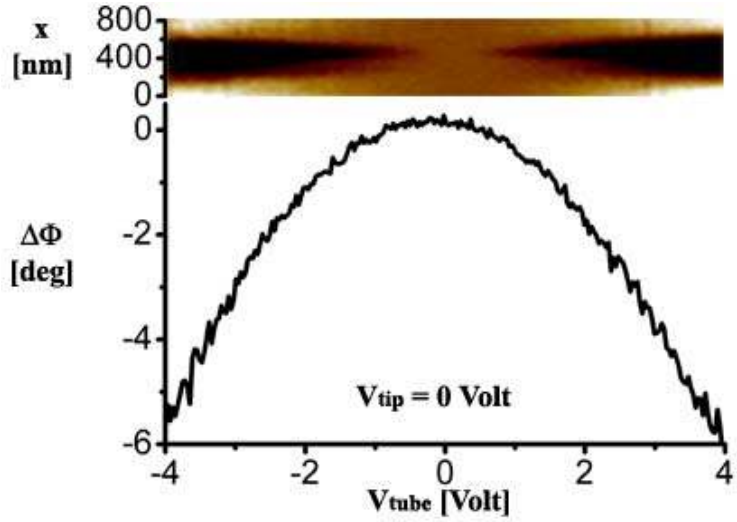

Figure S11. Effect of bias applied to nanotube on EFM contrast. The upper graph shows the dependence of EFM contrast ($\Delta\varphi$) as a function of bias (V_{tube}) and position across a nanotube serpentine segment (x). The lower graphs shows the dependence of EFM contrast ($\Delta\varphi$) on bias (V_{tube}) when the tip is located 30 nm above the nanotube. The graph shows the typical parabolic shape that is symmetric about $V_{tube} = 0$.

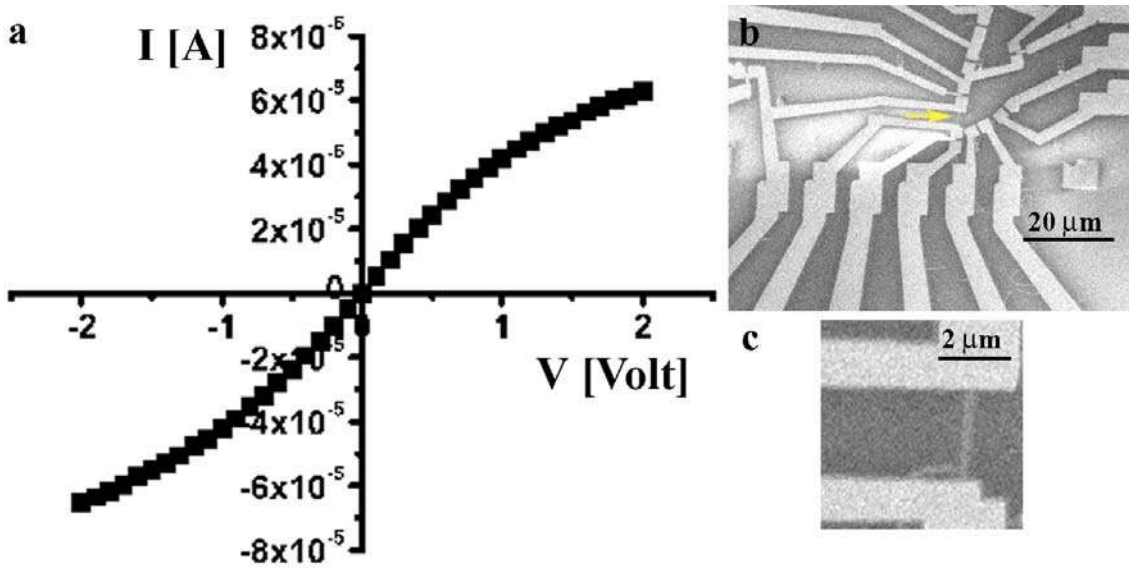

Figure S12. Near-ballistic conduction across a 2 μm serpentine segment. **a**, I-V curve from a DC measurement (see Methods). The resistance is 35 kΩ, which is only five times larger than the quantum resistance (6.5 kΩ). **b**, SEM

image of the area showing the electrical contacts pattern, bright, made on the nanotubes, yellow arrow shows the nanotube measured in **a**. **c**, enlarged image showing the nanotube of 2.5 μm length, connected to the Ti/Pd electrodes.

Data analysis and discussion about the 'falling spaghetti' mechanism

Here we analyse the serpentine shapes from a mechanical and aerodynamic point of view, and make some quantitative estimations (referred in the text), which are relevant to the discussion about the 'falling spaghetti' mechanism (Fig. 1 and movie).

Following the worm-like-chain model, the persistence length of a nanotube is given by eq. S1, where d is the nanotube diameter, k_BT is the thermal energy, and C is the in-plane stiffness of the rolled-up graphene layer (C = 345 N/m)[22]. Using the geometric data from the two serpentines of Fig. 3 at 800 °C, we obtain the values L_p = 25 μm and 145 μm, stated in the text. According to the theory, the typical diameters of random loops caused by Brownian motions should be around $D = 2L_p$ = 50 μm and 290 μm, which are one to two orders of magnitude larger than the actual U-turn diameters, D = 2.1 μm and 3.2 μm, respectively.

$$L_p = \pi C d^3 / 8 k_B T \qquad \text{(S1)}$$

The force that is necessary to exert on a nanotube opposite to the direction of zipping on a surface in order to form a suspended loop of diameter D for a nanotube diameter d, as depicted in Fig. S13, is derived from classical beam theory. The mechanical energy of a bent beam is given by eq. S2, where Y, I and R are the Young's modulus, the geometric moment of inertial, and the radius of curvature, respectively, of a beam element of contour length $d\ell$. The loop force is equal to the gradient of the mechanical energy for pulling the end of the suspended nanotube, i.e. eq. S3. The geometrical moment of inertia for a cylindrical beam is given by eq. S4, where r_{out} and

r_{in} are the outer and inner radius of the cylinder, respectively. For a thin cylinder, this can be approximated to $I = \pi r^3 \delta r$, where δr is the cylinder thickness. Considering that the in-plane stiffness of the rolled-up graphene layer is $C = Y\delta r$, and that $d = 2r$, this can be rewritten as eq. S5. Using the geometric data from Fig. 3, we obtain the values F_{loop} = 0.17 pN and 0.41 pN, stated in the text.

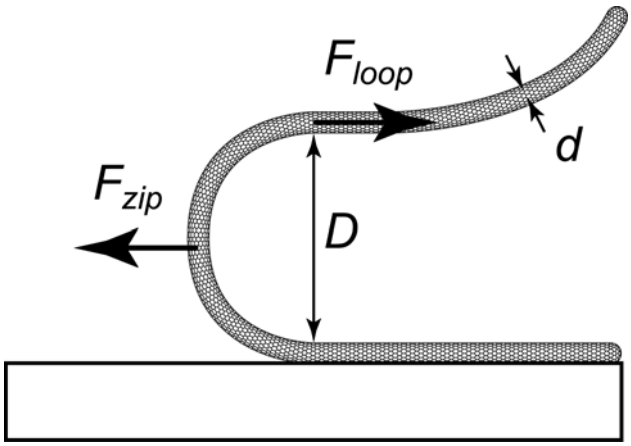

Figure S13. Schematic representation of the loop force F_{loop} and the zipping force F_{zip} for a suspended nanotube loop of diameter D and nanotube diameter d zipping along a surface.

$$E_m = \int \frac{YI}{2R^2} d\ell \qquad \text{(S2)}$$

$$F_{loop} = \frac{\partial E_m}{\partial \ell} = \frac{YI}{2R^2} \qquad \text{(S3)}$$

$$I = \frac{\pi (r_{out}^4 - r_{in}^4)}{4} \qquad \text{(S4)}$$

$$F_{loop} = \frac{\pi C d^3}{4D^2} \qquad \text{(S5)}$$

The driving force for the zipping of the nanotube along the surface is the work of adhesion per unit of nanotube length. The calculated van der Waals interaction energy between a single-wall nanotube of diameter 1.4 nm and an amorphous SiO_2 is 2 eV/nm[24]. Assuming that the interaction on a step of quartz is comparable to this value, then the equivalent 'zipping force' is 320 pN, as stated in the text. This is 3 orders of magnitude larger than the loop force. However, we should consider that the instability that leads to the formation of the loop does not necessarily take place when the drag force overcomes the zipping force, but when it overcomes an anisotropy energy per unit of nanotube length, which is necessary to 'derail' the nanotube from the step. If this attributed to the nanotube-surface interaction along a step relative to the nanotube-surface interaction along a different direction, and compare it to the loop force F_{loop}, then the corresponding anisotropy energy per nanotube length is 1.0 - 2.6 meV/nm for d = 1.4 and 2.5 nm, respectively (Fig.3a-g). According to the nearly linear dependence of D on d in Fig. 3h, and applying eq. S5, the anisotropy energy scales linearly with the d, with a factor 1.7 meV/nm^2.

We can roughly estimate the speed of the nanotube fall by comparing the estimated drag force opposed to zipping, which is revealed by the loop force, and a theoretical drag. Assuming that the zipping is faster than the flow near the surface, then the major drag component is due to the oscillatory sidewise motion of the suspended part of the nanotube along the step (x direction) during zipping. According to classical hydrodynamics at low Reynolds numbers, the drag force across a cylinder is given by eq. S6 (Ref.: H. Lamb, *Hydrodynamics*, Dover Publications, New York, 1945), where ρ is the fluid density, d and L are the cylinder diameter and length, v is the motion velocity, and C_D is the drag coefficient. The latter is given by eq. S7, where γ is the Euler's constant (γ = 0.57721665) and Re is the Reynolds number based on the cylinder diameter, given by eq. S8, where η is the fluid viscosity.

$$F_d = \frac{1}{2} C_D \rho d L v^2 \quad \text{(S6)}$$

$$C_D = \frac{8\pi}{1/2 - \gamma - \ln(Re/8)} \quad \text{(S7)}$$

$$Re = \frac{\rho v d}{\eta} \quad \text{(S8)}$$

Using the viscosity of Ar and H_2 (η = 563 and 200 μP at 825 ºC, Ref.: *CRC Handbook of Chemistry and Physics*, CRC Press, Boca Raton, Florida, USA, 1980) the weighed average viscosity of the mixture (60% Ar and 40% H_2) is η = 425 μP. Using the ideal gas law, ρ = 0.28 Kg/m^3. Taking a typical serpentine, we can assume d = 1.5 nm, D = 2 μm and W = 10 μm, with 20 oscillations (U-turns on each side). The effective length L of suspended nanotube that feels the drag is unknown. We can assume that the projected length of nanotube that moves at a significant velocity is somewhere between the serpentine width W = 10 μm and the full contour length L_c = 400 μm. Comparing the drag F_d to the loop force F_{loop} and using eq. S5-S8, we can roughly estimate the zipping speed to be v_{max} = 1-7 m/s. Then, the total zipping time that it should take for the whole nanotube to fall as a serpentine ranges 300 - 50 μs, and the frequency of the oscillations ranges 50 - 300 kHz, as stated in the text.

In these estimations, we neglected the drag component along the gas flow (y direction). The mean flow velocity in our experiments for the used flow rates 250 - 2000 sccm in a tube reactor of diameter 2.2 cm ranges 0.011 - 0.088 m/s. Although this is small compared to the estimated zipping velocity, and should be even smaller near the surface, it is only a small region of the suspended nanotube near the surface which feels the x-component drag, whereas the y-component drag is felt by the entire suspended nanotube, especially its upper regions, where laminar flow is faster. Therefore the y-component drag can be significant, causing the suspended loop to increase its actual

diameter before it falls. This would explain the observed dependence of the U-turn diameter on the flow rate, as well as the observed dependence of serpentine shape on the flow direction (Fig. 2). The observed decrease in U-turn diameter toward the end of the serpentines (Figs. 1 and S2) could be attributed to a gradual decrease in the drag component in the flow direction as the length of suspended part of the nanotube decreases. The observed increase in serpentine width toward the end of the serpentine could be attributed to a decrease in the drag component along the steps as the length of the suspended nanotube decreases, which means that the zipping must propagate farther from the centre of mass to reach the critical drag that derails the nanotube from the step to make a U-turn. The disorder at the end of some of the serpentines may be related to the gradual decrease in aerodynamic drag as the suspended part of the nanotube becomes shorter, because this reduction of damping could eventually push the non-equilibrium system from the oscillatory regime to a chaotic regime.

This analysis can qualitatively explain the available observations, however there might be additional considerations complicating the picture: (i) Classical aerodynamics might be quite inaccurate at the present length scales. (ii) The system might not be fully overdamped, in which case inertia and acceleration may not be neglected. (iii) The oscillations of the lower part of the nanotube during adsorption could also excite flexural waves propagating upwards along the suspended part of the nanotube, presetting a serpentine geometry in the suspended nanotube prior to its fall. (iv) Turbulences in the reactor or around the nanotube might further complicate the picture.

Although the details of the serpentine formation mechanism might be rather complex, we suggest that they could in principle be simulated with a relatively simple set of assumptions and parameters, considering the anisotropic nanotube-surface interactions, the nanotube-gas interactions, the nanotube mechanical properties, and the gas flow dynamics. Such simulations are beyond the scope of the present study.

Methods

Serpentine synthesis: For the serpentine nanotubes growth, one-side polished single-crystal quartz wafers (Sawyer Research Products, Inc.) were used. These vicinal α-SiO_2 $(1\bar{1}01)$ substrates were Y-cut with rotation angles of 32^0 (Figs. 1f, 2a-d and f-g, 3, S1a, c and f, S6a-b) and $42^0$45' (Figs. 1a-e, 2e,h, 4, S1b,d,e, S3, S4, S7 and S8) around the X-axis, except of Fig. S9, for which sapphire substrates (Monocrystal, miscut c-plane 2º or 4º toward the $[11\bar{2}0]$ direction) were used. The substrates were cleaned by sonication in acetone for 10 min before annealed for 8 h at 900 ^{0}C in air. Parallel stripes (25 μm wide, 10 nm thick) of amorphous SiO_2 (Kurt J.Lesker, 99.99%) were laid down in the surface step direction by a photolithography and electron-beam evaporation. Deposition of aqueous solution of ferritin (the growth catalyst) with concentration of 0.1-0.5μg/μl for 10 min. prior to lift-off in hot acetone (5 min.), followed by oxygen plasma of 100 W for 3 min, left the silica stripes patterned with the catalyst with almost no ferritin on the quartz itself. The growth of the nanotubes was performed by catalytic chemical vapour deposition (CVD) as previously reported[13,15,16,20]. Briefly, samples were placed inside the middle of a quartz tube (inner diameter 2.2 cm) at a defined angle α between the surface steps and the gas flow (typically 90^0, unless otherwise stated). The tube was placed in a furnace, and CVD was carried out at 800 °C and 1 atm with a mixture of 60% Ar, 40% H_2, 0.2% C_2H_4 at flow rates ranging from 250-2000 sccm (cm^3/min, typically 1000sccm, unless otherwise stated) for growth times ranging from 10-60 min (typically 10 min, unless otherwise stated). An alternative CVD procedure yielding serpentines in very high yields was using a nominally 0.5 nm thick evaporated layer of Fe (Kurt J.Lesker, 99.95%) on 30 nm-thick evaporated amorphous SiO_2 stripes. In this case, lift-off was done by weak sonication in acetone, Fe particles were oxidized at 550 ºC for 20 min. in air, and CVD was carried out at 900 °C and 1 atm for 60 min from a mixture of 60% Ar, 40% H_2, 0.4% C_2H_4 at flow rate of 500 sccm.

Measurements: The grown serpentines were characterized using field-emission scanning electron microscope (SEM, Supra 55VP FEG LEO and Ultra 55 Zeiss, Oberkochen, Germany, low working voltages of 0.5-2kV) and atomic force microscope (AFM, Veeco, Multimode Nanoscope IV). AFM scanning was carried out in air tapping mode using 70 kHz (FESP1) and 300 kHz (RTESP7) silicon tips (Nanoprobes). *Ex situ* TEM characterization of the nanotubes grown in our CVD process was performed in a FEI (Philips) Tecnai F30 U-Twin (300kV, FEG). The nanotubes were grown in the standard conditions described above from evaporated Fe (0.5 nm) on amorphous SiO_2 (30 nm), suspended in a small volume of ethanol by brief sonication, and deposited on lacy carbon-coated Cu grids for the HRTEM characterization. For the optical *in situ* characterization, we used a confocal Raman microscope as described previously (Ref. A. Hartschuh, H.N. Pedrosa, L. Novotny and T. D. Krauss, Science **2003**, *301***,** 1354-1356).

Electrostatic force microscopy (EFM) measurement were performed on samples containing serpentines that were grown under the described procedure and were connected to contact electrodes that were produced by depositing 5 nm Cr (Kurt J.Lesker, 99.95%) and 70 nm Au (Metalor, 99.999%) by electron-beam evaporation through a shadow mask containing 'L' shape and marking letters. SEM was used to locate the pads that fell on serpentines and they were wire-bonded to outer electrodes on a chip carrier. Ti/Pt coated tips (frequency ~70 kHz) were used for the EFM in lift-mode with an elevation of 20-30 nm. A bias ranging from -5 V to 5 V was applied to the electrode connected to one end of the serpentine, while the tip is grounded, and the phase shift of the tip oscillation was imaged as a function of tip position for each applied bias. To observe the phase shift as a function of the applied bias (Fig S7), the slow scan axis was disabled so the tip retraces the same nominal line across the nanotube, while varying the applied bias to the nanotube. Similar experiments were

performed applying a bias to the tip, while the serpentine contact electrode was grounded, and yielded similar results.

Transport measurements were carried out in DC mode at room temperature and ambient conditions using an electrical probe station (Kithley 235 source meter unit). A two-step electron-beam lithography process was done to create alignment marks and to locate the serpentines (15-20 nm of Au was thermal evaporated on top of the PMMA layers before each electron beam lithography step). After the first step, a layer of 5 nm Cr and 50 nm Au was electron-beam evaporated for the alignment marks, and after the second lithography step, the electrodes were created by electron beam evaporation of 0.2 nm Ti (Kurt J.Lesker, 99.995%) and 30 nm Pd (Holland-Moran, 99.95%). For very high density samples the first electron-beam lithography process was skipped and contacts were made randomly on the sample.